Title
Electric-Field-Induced Protein Translocation via a Conformational Transition in SecDF: An MD Study

Journal
Biophysical Journal, 112(12)

ISSN
0006-3495

Authors
Ficici, Emel
Jeong, Daun
Andricioaei, Ioan

Publication Date
2017-06-01

DOI
10.1016/j.bpj.2017.04.034

Peer reviewed

Biophysical Journal
Article

Biophysical Society

Electric-Field-Induced Protein Translocation via a Conformational Transition in SecDF: An MD Study

Emel Ficici,[1] Daun Jeong,[1] and Ioan Andricioaei[1,*]
[1]Department of Chemistry, University of California, Irvine, Irvine, California

ABSTRACT SecDF is an important component of the Sec protein translocation machinery embedded in the bacterial membrane, which is associated with many functions, such as stabilizing other Sec translocon components within the membrane, maintaining the transmembrane (TM) potential, and facilitating the ATP-independent stage of the translocation mechanism. Related studies suggest that SecDF undergoes functionally important conformational changes that involve mainly its P1-head domain and that these changes are coupled with the proton motive force (Δp). However, there still is not a clear understanding of how SecDF functions, its exact role in the translocation machinery, and how its function is related to Δp. Here, using all-atom molecular dynamics simulations combined with umbrella sampling, we study the P1-head conformational change and how it is coupled to the proton motive force. We report potentials of mean force along a root-mean-square-distance-based reaction coordinate obtained in the presence and absence of the TM electrical potential. Our results show that the interaction of the P1 domain dipole moment with the TM electrical field considerably lowers the free-energy barrier in the direction of F-form to I-form transition.

INTRODUCTION

An important mechanism in the infection of host cells by bacterial virulence factors is the translocation of unfolded secretory proteins across bacterial membranes (1). One such translocation mechanism is the Sec pathway (2–5). The Sec pathway is the common pathway between prokaryotes and eukaryotes in the translocation of secretory or plasma membrane proteins across the membrane. In prokaryotes, translocation occurs through the plasma membrane, whereas in eukaryotes it occurs through the endoplasmic reticulum membrane (4). The Sec translocon machinery is a protein-conducting channel that functions not only to translocate unfolded proteins across the plasma membrane but also to insert proteins into the membrane (2,6).

In many bacteria, the Sec machinery is composed of SecYEG (7,8), the core of the complex forming a protein-conducting channel, SecA ATPase (1,2), which initiates the translocation through binding of ATP, and SecDF, which is thought to facilitate the translocation in the later stages. In some organisms, SecDF is found as two closely interacting proteins, i.e., Sec D and SecF, and in others it is formed by a single chain (9).

Studies show that SecDF is functional in various stages of protein translocation. For example, it is thought to stabilize other components of the Sec machinery, i.e., SecY (10) and the membrane-inserted state of SecA (11–13). It also regulates protein translocation by stabilizing the translocation intermediates and by preventing their backward movement (13). SecDF is also important in the release of preprotein to the periplasmic side (14). Besides its direct role in protein translocation, as mentioned, SecDF is also required for the maintenance of proton motive force levels, which are needed for efficient translocation (13,15). It is due to these and related functions that the lack of SecDF results in severe growth retardation and defects in protein export in vivo (16,17). Moreover, its important role in the translocation of several virulence factors, and hence in the bacterial infection process, makes SecDF an important possible drug target for preventing bacterial infections. Also, because of its possible role in protein folding, understanding how SecDF functions is fundamentally relevant.

Despite its significant role in facilitating protein translocation, protein folding, and membrane protein insertion, the mechanism of SecDF function remains largely unexplored. One aspect that is clear is that SecDF functions in combination with the proton motive force, Δp, which is the electrochemical potential difference of protons across the membrane (18). It is known that both chemical and

Submitted September 19, 2016, and accepted for publication April 25, 2017.
*Correspondence: andricio@uci.edu
Editor: Anatoly Kolomeisky.
http://dx.doi.org/10.1016/j.bpj.2017.04.034

electrical components of the proton motive force, i.e., the pH gradient, ΔpH, and the transmembrane (TM) electric potential, $\Delta\psi$, respectively, have a direct role in the effective functioning of SecDF (19). ATP and the proton motive force act at different parts of the preprotein translocation catalytic cycle (19,20). ATP binding to SecA initiates the translocation. ATP hydrolysis later provides the release of the unfolded protein. The proton motive force acts at later stages to prevent the backward movement of the preprotein and it drives the rapid and efficient forward translocation reaction. The coupling of SecDF function to the proton motive force suggests that SecDF must undergo a conformational change driven by the proton motive force for it to function.

In a recent study, the structure of SecDF from *Thermus thermophilus* HB8 (TtSecDF) shows, indeed, two different conformations, the so-called F-form and I-form (21,22) (see Fig. 1). The two conformations vary by the relative positioning of a P1-head subdomain—the large periplasmic domain of TtSecDF—which is suggested to undergo a hinge motion. An analysis of SecDF structure using electron tomography and single-particle reconstruction (23) also supports the existence of two conformations consistent with the F-form and I-form structures reported earlier (22). The latter study also confirms the conformational flexibility of the P1 head relative to other domains, as predicted by the former study.

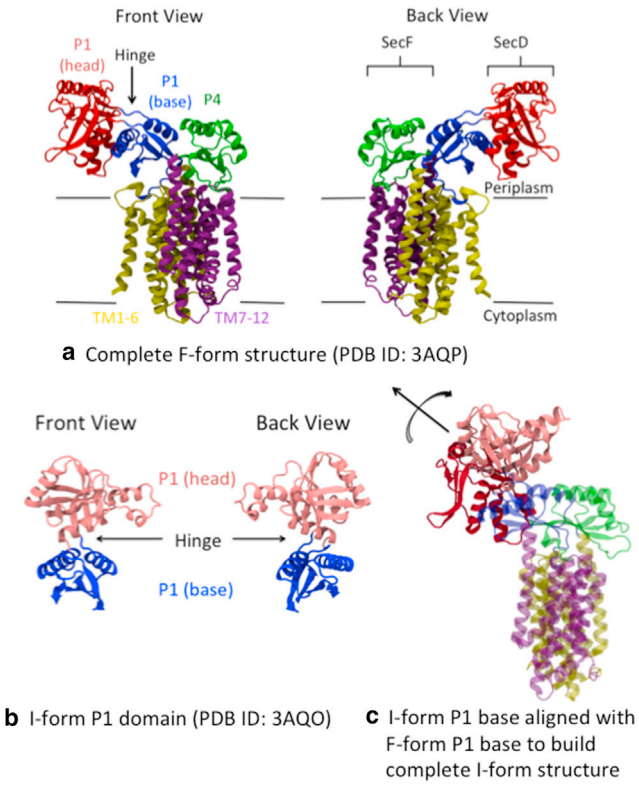

FIGURE 1 The two conformations of SecDF, (*a*) F-form and (*b*) I-form, differ by the positioning of the P1-head domain on the P1-base domain. The F-form and I-form P1-head subdomains are shown in red and pink, respectively. (*c*) The complete I-form structure is built by superimposing the I-form P1 base subdomain onto the corresponding subdomain of the F-form structure and appending the missing domains from the F-form structure. To see this figure in color, go online.

Although it is known that proper functioning of SecDF depends on the proton motive force and a conformational change driven by the proton motive force, the exact mechanism of how the two are coupled is not known. In this study, we find possible low-energy pathways for the SecDF conformational transitions in both directions, i.e., F-form to I-form and I-form to F-form, using the targeted molecular dynamics (TMD) method. To understand the role of proton motive force and how it influences the transition, we also study the conformational transitions in the existence of the TM electrostatic potential component of the proton motive force, which we modeled by applying a constant electric field. In addition, through potential-of-mean-force (PMF) calculations along the conformational transition pathways, we show that the interaction of the dipole moment of the SecDF P1-head with the TM potential significantly lowers the barrier for the F-to-I transition, and makes the I-form energetically more favorable. This can explain the source of the driving force needed for SecDF to carry the translocation intermediates from inside the channel, after capturing them while in the F-form, into the periplasm, as it transitions into the I-form conformation. With the depletion of the TM potential, i.e., in the absence of a potential gradient, the barriers for transition in both directions appear to have similar values.

In the following sections, we first briefly describe the TMD and umbrella sampling methods as we used them in this study. Next, we explain the details of the structure setup and simulations. Finally, we present and discuss our results, followed by concluding remarks.

MATERIALS AND METHODS

Targeted MD

Large-scale biomolecular conformational changes, such as the proposed transition between F-form and I-form conformations of SecDF, usually occur within timescales that are beyond the reach of equilibrium computational methods. Therefore, non-equilibrium methods are often used to gain qualitative insights about the transition pathways. In this study, the TMD method is used to find low-energy pathways for conformational transitions between the F-form and I-form. TMD is a method developed to induce conformational transitions via imposing holonomic constraints that minimize the root mean-square distance (RMSD) toward a target conformation while integrating MD trajectories at ordinary temperatures (24,25).

Since TMD is a non-equilibrium method, the resulting pathway is irreversible and it may result in non-physiological pathways, for example, by causing larger changes to occur before smaller ones (26). This may result in a seeming hysteresis between transitions in the forward and reverse directions, yet it may also be a useful method for generating several putative pathways, where the hysteresis is seen as the coexistence of pathways with different functional weights. Nevertheless, after obtaining a plausible pathway via TMD, more accurate free-energy estimates can later be made, and equilibrium properties can then be calculated by additional

methods such as umbrella sampling simulations. TMD has been successfully applied to study a variety of large-scale conformational changes for proteins (27–34) and nucleic acids (35–37). In this method, the evolving holonomic constraint of the form below is used to drive the system from an initial configuration $(\vec{r}_{\text{init}})$ to a target configuration $(\vec{r}_{\text{final}})$:

$$\phi(\vec{r}_t) \equiv \left(\text{RMSD}\left(\vec{r}_t, \vec{r}_{\text{final}}\right)\right)^2 - \rho(t)^2 = 0, \tag{1}$$

where $\rho(t)$ is an evolving RMSD that is initially set equal to the mass-weighted RMSD of the initial structure from the target structure, i.e., $(\text{RMSD}(\vec{r}_{\text{init}}, \vec{r}_{\text{final}}))$. To drive the structure toward the target structure, $\rho(t)$ is monotonically decreased until it is close to zero. Here, $\vec{r}_{\text{init}}$, $\vec{r}_{\text{final}}$, and $\vec{r}_t$ are 3N-dimensional configurational vectors of the N-atoms for initial structure, final structure, and intermediate structure, respectively, at time t. RMSD values between initial and final structures are calculated by

$$\text{RMSD}\left(\vec{r}_{\text{init}}, \vec{r}_{\text{final}}\right) = \sqrt{\frac{1}{\sum_{k=1}^{N} m_k} \sum_{k=1}^{N} m_k \left|\vec{r}_{k,\text{init}} - \vec{r}_{k,\text{final}}\right|^2}. \tag{2}$$

Satisfying the constraint given in Eq. 1 results in an additional constraint force, F^{c}, which is given by

$$F^{\text{c}} \equiv \lambda \frac{d\phi(\vec{r}_t)}{d\vec{r}_t} = 2\lambda\left(\vec{r}_t - \vec{r}_{\text{final}}\right). \tag{3}$$

The value of the parameter λ that satisfies the constraint is determined at each integration step.

Free-energy profiles

Once a plausible reaction pathway for the conformational transition is obtained, the PMF (38) along the pathway's progress variable can be calculated in principle from the probability distribution functions obtained through extensive sampling (39,40). In practice, however, advanced sampling techniques such as the venerable umbrella sampling technique are used to overcome the problem of insufficient sampling in the regions of high energy (41). In umbrella sampling, the reaction coordinate is covered by a series of adjacent and overlapping probability distribution windows in configuration space. Separate simulations for each window are performed while the system is restrained to the corresponding reaction-coordinate value by an additional harmonic biasing potential centered on that window. After the biased probability distributions are obtained by histogramming, they are unbiased using the weighted-histogram analysis method (WHAM) (42,43).

In our study, the PMF along the pathway that connects the two SecDF conformations, i.e., F-form and I-form, is calculated using the following biasing potential, $(w_{b,i})$, for each ith umbrella sampling window:

$$w_{\text{b},i} = K_i(\Delta\text{RMSD}(\vec{r}_t) - \Delta\text{RMSD}(\vec{r}_0))^2, \tag{4}$$

where ΔRMSD is defined as

$$\Delta\text{RMSD}(\vec{r}) = \text{RMSD}(\vec{r}_t, \vec{r}_F) - \text{RMSD}(\vec{r}_t, \vec{r}_I), \tag{5}$$

with $\text{RMSD}(\vec{r}_t, \vec{r}_{\text{F}})$ and $\text{RMSD}(\vec{r}_t, \vec{r}_{\text{I}})$ represent the RMSD values of the instantaneous structure from the initial equilibrated F-form and I-form structures, respectively. $\Delta\text{RMSD}(\vec{r}_0)$ is the minimum of the harmonic biasing potential. The choice of this one-dimensional order parameter, $\Delta\text{RMSD}(\vec{r})$, maintains the difference between RMSD values with respect to two reference structures around the given minimum while allowing relaxation in the RMSD value with respect to each reference structure. This form of biasing potential has previously been used, for example, to obtain the free-energy profile between B-form and A-form DNA structures (36,44).

Dipole-moment calculation

To understand how the SecDF conformational change involving the P1-head subdomain may be coupled with the proton motive force, we monitored the dipole moment of this subdomain along the TMD trajectories. The P1-head includes four α-helices, and protein α-helices are known to have net dipole moments along the helix axis arising from the additivity of the individual peptide bonds (45–47). By definition, the dipole moment $(\vec{\mu})$ of a protein or a domain is calculated from the position vector $(\vec{r})$ and the partial charge (q_j) of each atom using (48)

$$\vec{\mu} = \sum_j q_j \vec{r}_j; \tag{6}$$

as always, when the sum of the charges is zero, the dipole moment is origin independent (48).

Although the dipole-moment values obtained from TMD trajectories are helpful in gaining insight about how different transition pathways compare, they are obtained under nonequilibrium conditions. To retrieve equilibrium values of the ensemble-averaged dipole moment along the reaction coordinate, trajectories from umbrella sampling simulations can be used by unbiasing (49). The unbiased $<\mu_z>_i$, i.e., the time-averaged z-component of the dipole moment of the P1-head subdomain for each simulation window, i, after reweighting is calculated as

$$\langle \mu_z \rangle_i = \frac{\sum_{j=1}^{N_i} \mu'_{z,j} \, e^{\beta w_{\text{b},j}}}{\sum_{j=1}^{N_i} e^{\beta w_{\text{b},j}}}, \tag{7}$$

where $w_{\text{b},j}$ is the biasing potential for the jth snapshot in window i, $\mu'_{z,j}$ is the z-component of the biased dipole-moment value for the same snapshot, and N_i is the total number of snapshots within window i.

Simulation methods: setup and equilibration of the end-point configurations

Coordinates for the full-length F-form were taken from the Protein Data Bank (PDB: 3AQP) (22). The coordinates of the missing residues in the P4 domain were generated after overlaying the P4 domain with the NMR solution structure of P4 (PDB: 3AQO). The rest of the missing coordinates are built by using INTCOR and the positions of all hydrogens were determined via the HBUILD facilities in CHARMM (50).

The full-length F-form was then oriented along the z-direction such that the two TM helices TM4 (residues 323–353) and TM10 (residues 619–651) were centered at $z = 0$ Å (see Fig. 1 *a*). The P1 domain of the I-form structure is available with PDB: 3AQO, as shown in Fig. 1 *b*. The full-length I-form was modeled by first superimposing the heavy backbone atoms of the P1 base (from PDB: 3AQO) with the corresponding region in the full-length F-form followed by appending the missing regions from coordinates of the repaired F-form structure. As seen in Fig. 1 *c*, the I-form differed from the F-form in the way the P1-head subdomain was positioned onto the P1-base subdomain.

Both the F-form and I-form were equilibrated under the same conditions. SHAKE (51) was used to fix bonds to hydrogen, allowing a time step of 2 fs. The velocity Verlet integrator was used with the Nosé thermostat to keep the temperature constant at 298.15 K. Generalized Born with a simple switching (GBSW) model (52,53) was used to simulate the solvent and membrane effects. Membrane thickness was set to be 31 Å centered at $z = 0$ Å, with a membrane switching length of 5 Å on each side. The surface-tension coefficient was set to a value of 0.03 kcal/mol/Å. Non-bonded interactions were

cut off at 12 Å, with smoothing function turned on at 10 Å. CHARMM22 all-hydrogen parameters for proteins with CMAP corrections optimized specifically for GBSW were used with CHARMM software (Chemistry at Harvard Macromolecular Mechanics), version c34b2 (50,54,55).

First the system was minimized briefly with 50 steps of steepest descent followed by 50 steps of ABNR in implicit solvent and membrane while the backbone heavy atoms were fixed. Then, a harmonic restraining force with a force constant of 60 kcal/mol/Å was applied to backbone heavy atoms and the system was again minimized until the change in energy was 0.01 kcal/mol and then heated briefly. This cycle of minimization and heating was repeated while gradually reducing the force constant at each cycle until all restraint was removed after 300 ps. The system was then equilibrated at a constant temperature for 30 ns. The same procedure was used separately to prepare the structures for both conformations while a constant electric field of strength 7.7 mV/Å was applied in the $-z$ direction. This electric field strength corresponds to a voltage of ~240 mV across the membrane thickness of 31 Å. The RMSD of the backbone heavy atoms with respect to the original structure after reorienting each frame with respect to the original structure was calculated to monitor equilibration (see Fig. 2).

Targeted MD simulation

The RMSD between the equilibrated F-form and I-form structures was 12.8 Å for the case when no electric field is applied and 13.5 Å for the case when the electric field is applied. For each of these cases, I-form and F-form structures were initially placed after a best-fit alignment of all atoms between the two structures. Then, separate simulations were run to pull each structure toward the other, yielding four simulations: 1) F-form to I-form with the electric field (f2i E); 2) I-form to F-form with the electric field (i2f E); 3) F-form to I-form with no electric field (f2i), and 4) I-form to F-form with no electric field (i2f). The TMD method as implemented in the CHARMM software package (50) was used with a pulling speed of 5 Å/ns and a time step of 1 fs. Artificial rotation was removed every 10 simulation steps. The system was weakly coupled to a heat bath at 298.15 K with a coupling constant of 0.5 ps (56). Equilibrated structures as described above were used. For each case, initial and target structures were aligned with respect to TM4 and TM10, the two longest helices at the center of the TM region. All the transitions studied were smooth, with no unusually high-energy structures encountered during the transition. The TMD simulations were stopped when the RMSD between a coordinate set and the target structure was equal to 0.2 Å. Sample movies for transitions from the F-form to the I-form and in the reverse direction are included in the Supporting Material. The P1-head dipole moment was calculated along each trajectory for a selection of residues 58–261, which has a zero net charge.

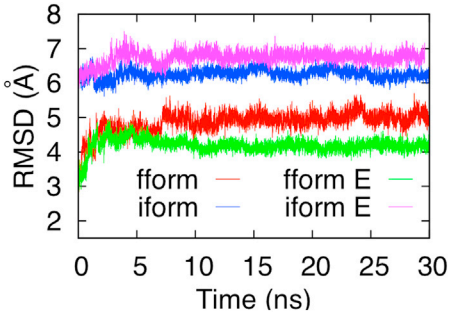

FIGURE 2 RMSD time series for the backbone heavy atoms during equilibration for each simulation: fform (*red*) and iform (*blue*) when there is no electric field, and fform E (*green*) and iform E (*purple*) when there is an electric field. Each frame is reoriented to give the best fit to the original structure. To see this figure in color, go online.

Umbrella sampling

Initial structures for each umbrella window were obtained from TMD trajectories by selecting snapshots with 0.2 Å RMSD between adjacent windows. To equilibrate each structure in each window, initial simulations were run with a higher biasing force constant of 200 kcal/mol/Å^2 for 20 ps. The force constant was gradually reduced to 10 kcal/mol/Å^2 over the course of 80 ps, after which additional equilibration was performed for 50 ps using this force constant. Finally, each umbrella sampling window was sampled for 3 ns. After obtaining biased probability distributions from the resulting trajectories, WHAM (42,43) was used to unbias the distributions and to obtain the PMF profile. Equilibrium averages of the dipole-moment z-component, μ_z, were calculated from umbrella sampling simulations after unbiasing according to Eq. 7.

RESULTS AND DISCUSSION

The RMSD of equilibrated F-form structures from the crystal structures reached a plateau at 4 Å when the electric field was applied and at 5 Å when the electric field was not applied (see Fig. 2). On the other hand, the RMSD for I-form structures reached a plateau at 7 Å when the electric field was applied and at 6 Å when the field was not applied. The relatively higher RMSD for I-form structures can be understood by the lack of a complete I-form structure. Since the only available structure for the I-form was the P1 domain, which had only the P1-base subdomain in common with the complete F-form structure, the I-form structure we built involved the assumption that the P1-base subdomain in the I-form had the same positioning with respect to the other domains as in the F-form. However, as pointed out in another study (23), it is possible that the P1 base subdomain in the two structures may initially have different positions relative to the other domains, which may explain the relatively high RMSD of the equilibrated I-form with respect to the originally built structure.

Fig. 3 shows superimposed structures of before and after equilibration for all cases. It can be seen that the P1-head subdomain in the equilibrated F-form structure lies slightly closer to the TM region than in the original F-form structure. For the I-form case, the equilibrated P1 domain appeared closer to the P4 domain than it was in the original structure.

Finding and characterizing conformational transition pathways

According to the TMD simulations, the SecDF conformational change involved the proposed hinge motion of the P1-head, as expected, i.e., via a rotational motion between F-form and I-form structures. Two movies of the conformational transitions between the F-form and I-form in each direction are included in the Supporting Material in mpg format. The P1-head includes four α-helices, which are known to have considerable dipole moments. Since the P1-head domain is roughly charge neutral, it will interact predominantly with the electric field through its dipole moment. Therefore, to investigate how the P1-head dipole

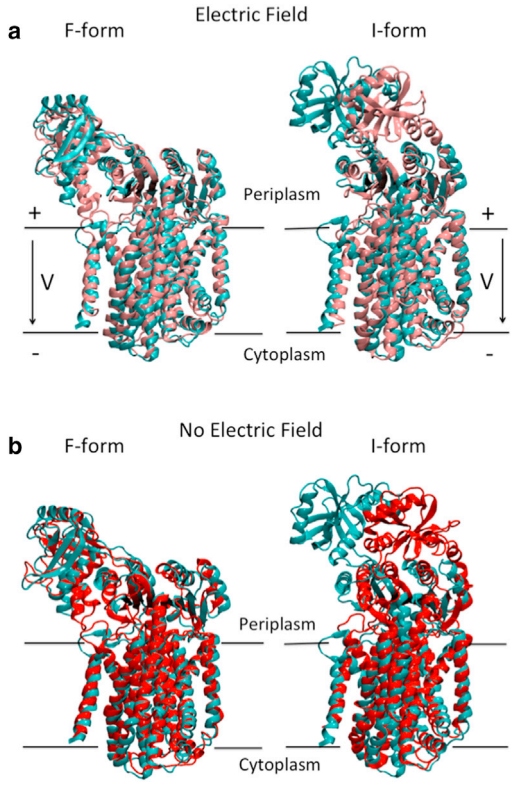

FIGURE 3 The equilibrated structures (*red*) of the two different SecDF conformations, (*a*) F-form and (*b*) I-form, are shown superimposed on the initial structures (*cyan*). To see this figure in color, go online.

moment ($\vec{\mu}$) couples with the electric field, we calculated the P1-head dipole moment for residues 58–261. This selection had a zero net charge, and therefore, the dipole moment values would be independent of the choice of a coordinate system. Since μ_x and μ_y were orthogonal to the electric field applied in the $-z$ direction, only the z component, μ_z interacts with the electric field. Thus, we plotted μ_z in Fig. 4 and found that all transition paths, except for the case of the F-to-I transition in the presence of an electric field, yielded similar trends of μ_z. On the other hand, the observed hysteresis indicates the possibility of a favorable interaction of the

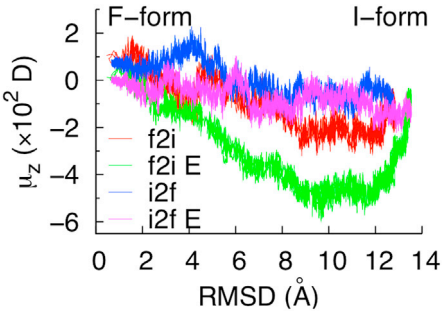

FIGURE 4 Dipole-moment z-component (μ_z) for the P1-head as obtained from TMD simulation trajectories. To see this figure in color, go online.

P1-head dipole moment with the electric field during the F-to-I transition when the electric field was applied. Further characterization of the transition is made through umbrella sampling simulations, as discussed in the next section.

Potential of Mean Force

To further investigate the conformational transition between the F-form and the I-form, as well as to understand the influence of the electric field on the transition, we obtained the PMF values along the conformational transition pathways defined by a ΔRMSD metric as explained earlier in the Materials and Methods. Accordingly, the reaction coordinate takes values between $\Delta\text{RMSD} = -12$ and 12 Å, which correspond to F-form and I-form conformations, respectively.

As seen in Fig. 5, the PMF obtained when no electric field was applied showed two minima near −8.7 (F-form-like structure) and 6.4 Å (I-form-like structure), with the latter minimum at ∼5 kcal/mol lower energy than the former minimum. The free-energy minimum near the F-form structure was narrower, reflecting the fact that the F-form conformation was more restricted in its motion than the I-form-like structures. This is likely due to the strong interaction of the two helices, shown in cyan in Fig. 6, with the TM helices in the F-form conformation. PMF profiles also revealed that the F-to-I transition was almost barrierless in the presence of the electric field. In this case, the I-form conformation had a much lower energy (−20 kcal/mol), with a wide low-energy basin. This indicates that the P1-head was highly mobile in this region, more so than in the previous case, where no electric field was applied. As a result, there were multiple low-energy structures in this region. Sample structures from each free-energy minimum are shown in Fig. 6. Some of these structures from umbrella sampling simulations aligned on the initial equilibrated structures are included in Figs. S3 and S4. The very high energy barrier in the reverse direction makes the F-form conformation highly unlikely in the presence of an electric field.

To understand the influence of the interaction of the P1-head dipole moment with the electric field applied in the $-z$ direction, we calculated $<\mu_z>$, the averaged dipole-moment z component for each umbrella sampling window after unbiasing. As shown in Fig. 7, the z-component of the P1-head dipole moment was about $100D$ lower when there was an electric field than when there was no electric field. Also in the I-form conformation, the P1-head dipole moment was oriented such that its interaction with the electric field through its dipole moment would be greater than in the F-form conformation.

To compare the overall effect of the electric field on conformational transitions regardless of the direction of transition, we then combined umbrella sampling data obtained from the F-form-to-I-form and I-form-to-F-form transitions to find the unbiased dipole moment. The two

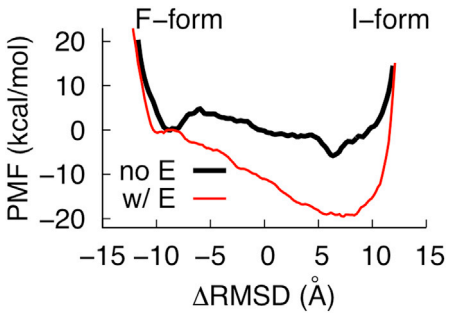

FIGURE 5 PMF profiles for the conformational transition between SecDF F-form and I-form when an electric field is applied (*red*) and when no electric field is applied (*black*). An assessment of convergence is included in the Supporting Material. To see this figure in color, go online.

cases, i.e., sampling obtained with and without the electric field, were treated independently. As seen in Fig. 7, the intermediate structures, i.e., structures in the region $-5 < \Delta\text{RMSD} < 5$ were found to have dipole moments lower than the F-form-like structures, which may help stabilize the intermediate structures more than F-form-like configurations. Moreover, I-form-like structures with $\Delta\text{RMSD} > 5$ were found to have an even lower dipole moment, which may cause the I-form structure to be even more stable than the intermediate, as well as F-form like structures. In the presence of an electric field, the P1-head dipole moment in the z-direction was consistently lower (more negative) throughout the reaction coordinate, maintaining a favorable P1-head dipole-moment-electric-field interaction. Therefore, we concluded that I-form like structures and the intermediate structures were stabilized through the interaction of the TM potential with the P1-head dipole moment and that this interaction facilitated the F-form-to-I-form conformational change and hence regulated the transition kinetics.

This result may explain why both the proton motive force and SecDF are necessary for effective translocation, as observed in the experimental studies. Accordingly, the conformational change from F-form to I-form is needed to prevent preprotein backward motion and to enhance its forward motion. This conformational change in turn relies on the interaction of the P1-head dipole moment with the TM potential, which stabilizes intermediate and I-form like structures. On the other hand, in the absence of the TM potential, this stabilizing effect will be lost and the kinetics needed for effective preprotein translocation will be distorted. This is consistent with the mechanism proposed earlier (22) that relates the I-form-to-F-form transition to proton flow, which would transiently reduce the accumulated TM potential.

P1 domain motion

To analyze the overall P1 domain motion during the conformational change, we calculated the principal moment of inertia for residues 31–263. To understand the relative motion of the P1 domain with respect to the rest of the protein, we defined angles ϕ and θ, as shown in Fig. 8 *a*. Accordingly, the angle ϕ was defined as the angle between the P1 domain principal axis and the principal axis of the main protein body excluding the P1-head, which was closely aligned with the z-axis. The angle θ was defined as the angle that the projection of the P1 domain principal axis onto the x-y plane makes with the x axis. Equilibrium averages of both angles, i.e., $\langle\phi\rangle$ and $\langle\theta\rangle$, were found from umbrella sampling simulations. Fig. 8 showed that the configurational change involved as much as a 40° increase in the angle $\langle\phi\rangle$ coupled with an increase of about 60° in the angle $<\theta>$, with both angles accompanied by large fluctuations.

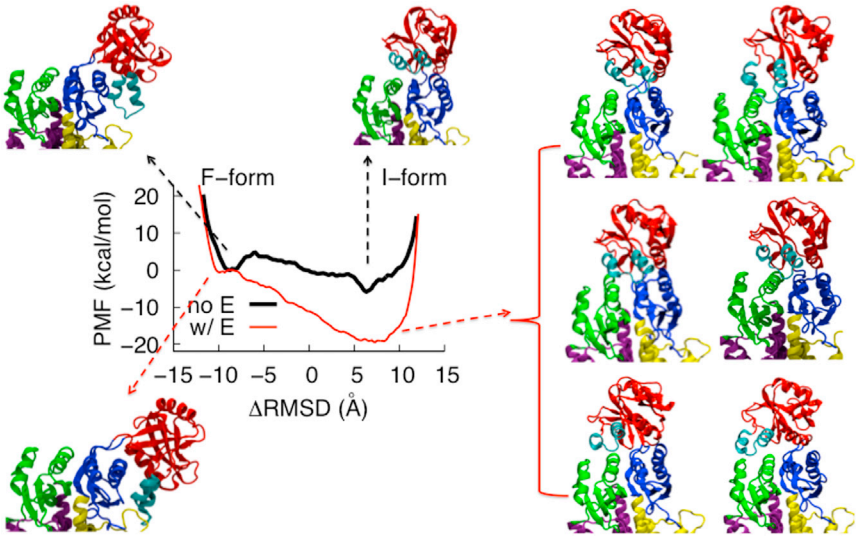

FIGURE 6 Sample minimum-energy structures near each minimum of the PMF profiles. To see this figure in color, go online.

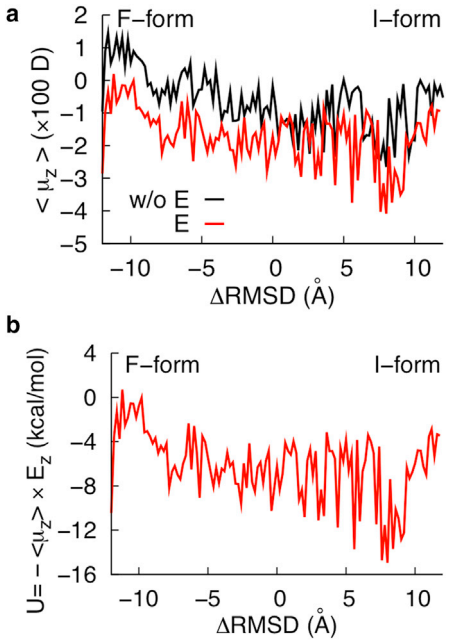

FIGURE 7 Unbiased averages for (*a*) μ_z, i.e., the *z*-component of the dipole moment from umbrella sampling simulations for the cases with and without an electric field, and (*b*) the energy of interaction between the protein P1-head subdomain dipole moment and the applied electric field. Transitions in each direction, i.e., F-form to I-form and I-form to F-form, are combined to compute unbiased equilibrium averages. To see this figure in color, go online.

CONCLUSIONS

In this study, we investigated the conformational dynamics of TtSecDF as it undergoes transitions between the F-form and I-form and how this conformational change was coupled with the proton motive force. We first explored transition pathways between the two conformations using all-atomistic TMD simulations. An analysis of the P1-head dipole moment along the transition pathways revealed a hysteresis between F-to-I and I-to-F transitions in the case of the existence of a TM potential. This indicated a coupling between the TM potential and the P1-head dipole moment. To estimate the free-energy profiles along the conformational transitions, we performed umbrella sampling simulations along a ΔRMSD-based reaction coordinate. A comparison of the PMF profiles obtained in the presence and in the absence of an electric field, which was used to simulate the TM potential effect, revealed that the TM potential indeed lowers the barrier significantly in the F-to-I transition pathway. A free-energy difference of about −18.3 kcal/mol between F-form and I-form conformations may provide the driving force needed for the P1-head to carry unfolded preproteins into the periplasm after capturing them in the SecYEG protein conducting channel.

The PMF profiles helped us explain the coupling between proton motive force and the SecDF conformational change. They further provided strong evidence for the following mechanism of function: SecDF captures preproteins from the channel in its F-form when the TM potential is in a depleted state. As the TM potential is formed, SecDF undergoes a conformational change from F-form to I-form and stays in the I-form conformation as long as the TM potential is maintained. The high free-energy barrier in the reverse direction makes the I-to-F transition highly unlikely when there is a TM potential. As the TM potential is temporarily depleted through the flow of protons across the SecDF TM channel, the F-form conformation becomes more easily accessible, since the difference in free energy drops from

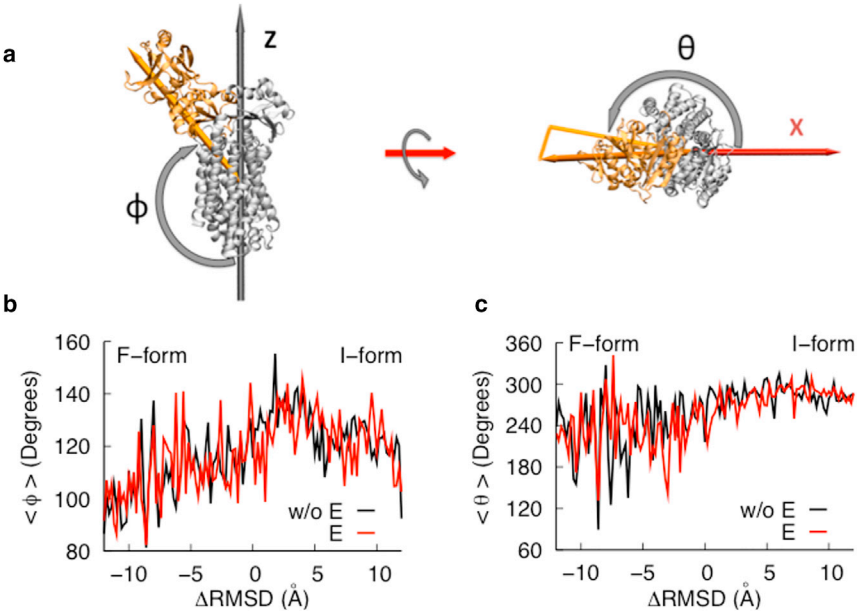

FIGURE 8 (*a*) Definitions of angles (ϕ and θ) used to characterize P1-head motion. (*b*) Equilibrium average of angle ϕ formed between the principal axes of the P1-domain and the TM domain (TM1–12). (*c*) Equilibrium average of angle θ formed between the projection of the P1-domain principle axis on the *x*-*y* plane and the *x* axis. To see this figure in color, go online.

20 kcal/mol when there is an electric field to ~5 kcal/mol when there is no electric field.

As a result, we can conclude that the favorable interaction of the P1-head dipole moment with the electric field due to the presence of a TM potential may explain the SecDF functional conformational change and how it is coupled to the proton motive force. Here, we need to note that this study includes only the electric TM potential component ($\Delta\psi$) of the proton motive force, Δp, and does not include the effects of pH gradient component (ΔpH) (or the difference in the concentration of ions or osmotic effect). The effects of ΔpH can be studied in detail by explicit-solvent simulations and by taking into account different protonation states of ionizable residues in the SecDF structure (57). Finally, our results, based on the interaction of the $\Delta\psi$ component of Δp with the SecDF P1-head subdomain, where the main component of the interaction would be given by the dipole-field term of the corresponding multipole expansion, can be experimentally tested by mutating residues that contribute to the P1-head dipole moment.

SUPPORTING MATERIAL

Four figures and two movies are available at http://www.biophysj.org/biophysj/supplemental/S0006-3495(17)30450-2.

AUTHOR CONTRIBUTIONS

E.F., D.J., and I.A. designed the research, E.F. conducted the research and analyzed the results, E.F. and I.A. wrote the article.

ACKNOWLEDGMENTS

We thank the National Energy Research and Scientific Computing Center and the Extreme Science and Engineering Discovery Environment for the computational resources made available to us by the U.S. Department of Energy and the National Science Foundation, respectively.

REFERENCES

1. Zimmer, J., Y. Nam, and T. A. Rapoport. 2008. Structure of a complex of the ATPase SecA and the protein-translocation channel. *Nature.* 455:936–943.
2. du Plessis, D. J. F., N. Nouwen, and A. J. M. Driessen. 2011. The Sec translocase. *Biochim. Biophys. Acta.* 1808:851–865.
3. Hand, N. J., R. Klein, …, M. Pohlschröder. 2006. Archaeal and bacterial SecD and SecF homologs exhibit striking structural and functional conservation. *J. Bacteriol.* 188:1251–1259.
4. Rapoport, T. A. 2007. Protein translocation across the eukaryotic endoplasmic reticulum and bacterial plasma membranes. *Nature.* 450:663–669.
5. Rapoport, T. A. 2008. Protein transport across the endoplasmic reticulum membrane. *FEBS J.* 275:4471–4478.
6. Gumbart, J. C., and C. Chipot. 2016. Decrypting protein insertion through the translocon with free-energy calculations. *Biochim. Biophys. Acta.* 1858 (7 Pt B):1663–1671.
7. Van den Berg, B., W. M. Clemons, Jr., …, T. A. Rapoport. 2004. X-ray structure of a protein-conducting channel. *Nature.* 427:36–44.
8. Tsukazaki, T., H. Mori, …, O. Nureki. 2008. Conformational transition of Sec machinery inferred from bacterial SecYE structures. *Nature.* 455:988–991.
9. Bolhuis, A., C. P. Broekhuizen, …, J. M. van Dijl. 1998. SecDF of Bacillus subtilis, a molecular Siamese twin required for the efficient secretion of proteins. *J. Biol. Chem.* 273:21217–21224.
10. Sagara, K., S. Matsuyama, and S. Mizushima. 1994. SecF stabilizes SecD and SecY, components of the protein translocation machinery of the *Escherichia coli* cytoplasmic membrane. *J. Bacteriol.* 176: 4111–4116.
11. Economou, A., and W. Wickner. 1994. SecA promotes preprotein translocation by undergoing ATP-driven cycles of membrane insertion and deinsertion. *Cell.* 78:835–843.
12. Economou, A., J. A. Pogliano, …, W. Wickner. 1995. SecA membrane cycling at SecYEG is driven by distinct ATP binding and hydrolysis events and is regulated by SecD and SecF. *Cell.* 83:1171–1181.
13. Duong, F., and W. Wickner. 1997. The SecDFyajC domain of preprotein translocase controls preprotein movement by regulating SecA membrane cycling. *EMBO J.* 16:4871–4879.
14. Matsuyama, S., Y. Fujita, and S. Mizushima. 1993. SecD is involved in the release of translocated secretory proteins from the cytoplasmic membrane of *Escherichia coli*. *EMBO J.* 12:265–270.
15. Arkowitz, R. A., and W. Wickner. 1994. SecD and SecF are required for the proton electrochemical gradient stimulation of preprotein translocation. *EMBO J.* 13:954–963.
16. Pogliano, J. A., and J. Beckwith. 1994. SecD and SecF facilitate protein export in *Escherichia coli*. *EMBO J.* 13:554–561.
17. Echizen, Y., T. Tsukazaki, …, O. Nureki. 2011. Crystallization and preliminary x-ray diffraction of the first periplasmic domain of SecDF, a translocon-associated membrane protein, from *Thermus thermophilus*. *Acta Crystallogr. Sect. F Struct. Biol. Cryst. Commun.* 67:1367–1370.
18. Shiozuka, K., K. Tani, …, H. Tokuda. 1990. The proton motive force lowers the level of ATP required for the in vitro translocation of a secretory protein in Escherichia coli. *J. Biol. Chem.* 265:18843–18847.
19. Driessen, A. J., and W. Wickner. 1991. Proton transfer is rate-limiting for translocation of precursor proteins by the *Escherichia coli* translocase. *Proc. Natl. Acad. Sci. USA.* 88:2471–2475.
20. Schiebel, E., A. J. Driessen, …, W. Wickner. 1991. Delta mu H^+ and ATP function at different steps of the catalytic cycle of preprotein translocase. *Cell.* 64:927–939.
21. Tsukazaki, T., H. Mori, …, K. Ito. 2006. Purification, crystallization and preliminary x-ray diffraction of SecDF, a translocon-associated membrane protein, from *Thermus thermophilus*. *Acta Crystallogr. Sect. F Struct. Biol. Cryst. Commun.* 62:376–380.
22. Tsukazaki, T., H. Mori, …, O. Nureki. 2011. Structure and function of a membrane component SecDF that enhances protein export. *Nature.* 474:235–238.
23. Mio, K., T. Tsukazaki, …, C. Sato. 2014. Conformational variation of the translocon enhancing chaperone SecDF. *J. Struct. Funct. Genomics.* 15:107–115.
24. Schlitter, J., M. Engels, …, A. Wollmer. 1993. Targeted molecular dynamics simulation of conformational change-application to the T-R transition in insulin. *Mol. Simul.* 10:291–308.
25. Schlitter, J., M. Engels, and P. Krüger. 1994. Targeted molecular dynamics: a new approach for searching pathways of conformational transitions. *J. Mol. Graph.* 12:84–89.
26. Ovchinnikov, V., and M. Karplus. 2012. Analysis and elimination of a bias in targeted molecular dynamics simulations of conformational transitions: application to calmodulin. *J. Phys. Chem. B.* 116:8584–8603.
27. Ma, J., T. C. Flynn, …, M. Karplus. 2002. A dynamic analysis of the rotation mechanism for conformational change in F(1)-ATPase. *Structure.* 10:921–931.
28. Ma, J., and M. Karplus. 1997. Molecular switch in signal transduction: reaction paths of the conformational changes in ras p21. *Proc. Natl. Acad. Sci. USA.* 94:11905–11910.

29. van der Vaart, A., J. Ma, and M. Karplus. 2004. The unfolding action of GroEL on a protein substrate. *Biophys. J.* 87:562–573.

30. Ma, J., P. B. Sigler, …, M. Karplus. 2000. A dynamic model for the allosteric mechanism of GroEL. *J. Mol. Biol.* 302:303–313.

31. Barbacid, M. 1987. *ras* genes. *Annu. Rev. Biochem.* 56:779–827.

32. Ford, B., V. Hornak, …, N. Nassar. 2006. Structure of a transient intermediate for GTP hydrolysis by ras. *Structure.* 14:427–436.

33. Hall, B. E., D. Bar-Sagi, and N. Nassar. 2002. The structural basis for the transition from Ras-GTP to Ras-GDP. *Proc. Natl. Acad. Sci. USA.* 99:12138–12142.

34. Diaz, J. F., B. Wroblowski, …, Y. Engelborghs. 1997. Calculation of pathways for the conformational transition between the GTP- and GDP-bound states of the Ha-ras-p21 protein: calculations with explicit solvent simulations and comparison with calculations in vacuum. *Proteins.* 28:434–451.

35. Aci, S., S. Mazier, and D. Genest. 2005. Conformational pathway for the kissing complex→extended dimer transition of the SL1 stem-loop from genomic HIV-1 RNA as monitored by targeted molecular dynamics techniques. *J. Mol. Biol.* 351:520–530.

36. Bascom, G., and I. Andricioaei. 2014. Single-walled carbon nanotubes modulate the B- to A-DNA transition. *J Phys Chem C Nanomater Interfaces.* 118:29441–29447.

37. Wereszczynski, J., and I. Andricioaei. 2006. On structural transitions, thermodynamic equilibrium, and the phase diagram of DNA and RNA duplexes under torque and tension. *Proc. Natl. Acad. Sci. USA.* 103:16200–16205.

38. Kirkwood, J. G. 1935. Statistical mechanics of fluid mixtures. *J. Chem. Phys.* 3:300.

39. Roux, B., and M. Karplus. 1991. Ion transport in a model gramicidin channel. Structure and thermodynamics. *Biophys. J.* 59:961–981.

40. Roux, B. 1995. The calculation of the potential of mean force using computer simulations. *Comput. Phys. Commun.* 91:275–282.

41. Torrie, G. M., and J. P. Valleau. 1977. Nonphysical sampling distributions in Monte Carlo free-energy estimation: umbrella sampling. *J. Comput. Phys.* 23:187–199.

42. Kumar, S., J. M. Rosenberg, …, P. A. Kollman. 1992. The weighted histogram analysis method for free energy calculations on biomolecules. I. the method. *J. Comput. Chem.* 13:1011–1021.

43. Grossfield, A. 2003. WHAM: the weighted histogram analysis method. Version 2.0.6. http://membrane.urmc.rochester.edu/content/wham.

44. Banavali, N. K., and B. Roux. 2005. Free energy landscape of A-DNA to B-DNA conversion in aqueous solution. *J. Am. Chem. Soc.* 127: 6866–6876.

45. Hol, W. G. 1985. The role of the α-helix dipole in protein function and structure. *Prog. Biophys. Mol. Biol.* 45:149–195.

46. Hol, W. G., P. T. van Duijnen, and H. J. Berendsen. 1978. The α-helix dipole and the properties of proteins. *Nature.* 273:443–446.

47. Wada, A. 1976. The α-helix as an electric macro-dipole. *Adv. Biophys.* 1976:1–63.

48. Antosiewicz, J. 1995. Computation of the dipole moments of proteins. *Biophys. J.* 69:1344–1354.

49. Becker, O. M., A. D. MacKerell, Jr., …, M. Watanabe. 2001. Computational Biochemistry and Biophysics. CRC Press, Florida.

50. Brooks, B. R., C. L. Brooks, 3rd, …, M. Karplus. 2009. CHARMM: the biomolecular simulation program. *J. Comput. Chem.* 30:1545–1614.

51. Ryckaert, J., G. Ciccotti, and H. J. C. Berendsen. 1977. Numerical integration of the cartesian equations of motion of a system with constraints: molecular dynamics of N-alkanes. *J. Comput. Phys.* 23:327–341.

52. Im, W., M. S. Lee, and C. L. Brooks, 3rd. 2003. Generalized born model with a simple smoothing function. *J. Comput. Chem.* 24: 1691–1702.

53. Im, W., M. Feig, and C. L. Brooks, 3rd. 2003. An implicit membrane generalized born theory for the study of structure, stability, and interactions of membrane proteins. *Biophys. J.* 85:2900–2918.

54. Brooks, B. R., R. E. Bruccoleri, …, M. Karplus. 1983. CHARMM: a program for macromolecular energy, minimization, and dynamics calculations. *J. Comput. Chem.* 4:187–217.

55. MacKerel, A. D., Jr., C. L. Brooks, III, …, M. Karplus. 1998. CHARMM: the energy function and its parameterization with an overview of the program. *In* The Encyclopedia of Computational Chemistry. John Wiley & Sons, pp. 271–277.

56. Berendsen, H. J., J. P. M. Postma, …, J. R. Haak. 1984. Molecular dynamics with coupling to an external bath. *J. Chem. Phys.* 81:3684–3690.

57. Goh, G. B., E. N. Laricheva, and C. L. Brooks, 3rd. 2014. Uncovering pH-dependent transient states of proteins with buried ionizable residues. *J. Am. Chem. Soc.* 136:8496–8499.